Journal of Porous Materials (2024) 31:577–586
https://doi.org/10.1007/s10934-023-01534-z

Mesoporous Zr@KIT-6 silicas: synthesis, characterization studies and catalytic application in the decomposition of hydrogen peroxide

Gamze Gunduz-Meric[1]

Accepted: 4 November 2023 / Published online: 27 November 2023

Abstract
H_2O_2 (hydrogen peroxide) is an effective and environmentally friendly material, and many studies have been carried out to develop new and efficient materials in recent years. Mesoporous silicas, especially KIT-6, is one of them, but there are few studies about it and its derivatives. In this study, KIT-6 silicas were synthesized hydrothermally using Pluronic P123 as a surfactant and n-butanol as a co-solvent in a mildly acidic condition. The Zr@KIT-6 silicas, prepared with various Si/Zr ratios (1.25, 2.5, 5, and 10 wt%), possess a high specific surface area (739–780 m^2/g). The synthesized materials were characterized by SEM, TEM, FT-IR, NH_3-TPD, H_2-TPR, ICP-OES, N_2 adsorption–desorption, and XRD methods. The surface area of the materials decreased with the increase of zirconium content in Zr@KIT-6. The high quality of cubic la3d silica was evaluated by TEM. Zr has effective and excellent performance for the H_2O_2 decomposition reaction. The results also showed that Zr-based KIT-6 silicas were stable and reusable materials over H_2O_2 decomposition tests. All the materials were found to be active (63–91% conversion) in the decomposition of H_2O_2 under mild conditions.

Keywords KIT-6 · Zirconium (IV) · H_2O_2 decomposition · Environmentally friendly

1 Introduction

Hydrogen peroxide (H_2O_2) is an environmentally friendly chemical because its by-products are only oxygen and water [1, 2]. Due to this, it is generally used in wastewater treatment, paper, petrochemical industries, fuel cells for space missions, etc. [3–5]. Metals such as Ag, Cu, Fe, Cr, Ni, Zr, Pt, Nb, and lanthanides or their silica form have been used for decomposition reactions [6–10]. The decomposition of the H_2O_2 reaction provides a clear route for producing unharmful and safe products [11, 12]. Homo- and heterogeneous catalysts have been widely used in the decomposition of H_2O_2 reactions [13–15]. This reaction is also technically important because of its energy conversion technology, such as aircraft jets, underwater vehicles, rockets, and missiles [16–18]. Peroxide has been utilized in increasing amounts in oxidation reactions that produce various fine and bulk chemicals [19]. Glycerol, cyclohexane, benzyl alcohol, and ethylbenzene are all extensively oxidized by hydrogen peroxide [20]. Since H_2O_2 usually occurs as an intermediate and participates in certain steps of the reaction pathway, its decomposition is important for study even in the context of other oxygen-based oxidations [21, 22]. The yield of the product reduces, and the reaction becomes limited when peroxide is broken down in water. Studying the role of the catalyst in peroxide decomposition is important for obtaining increased peroxide usage and enhanced product yield in the oxidation process. Previous studies reported that the decomposition of H_2O_2 is faster with metal-supported catalysts [9, 10, 23, 24]. The study gave an insight into the role of metals in the examination of the decomposition reaction to enhance its performance.

Porous silicas with high specific areas, such as MCM-41, MCM-48, SBA-15, SBA-16, SBA-12, SBA-2, SBA-1, KIT-5, KIT-6, etc. [25–27], are very useful and have been developed over recent years. These materials contain transition metal ions due to a direct hydrothermal synthesis method that prevents pore blockages by distributing the heteroatoms uniformly throughout the framework instead of incorporating them as metal-oxide particles. Although MCM-41 and SBA-15 type silicas have received the most attention, we have recently demonstrated that KIT-6 structures with ordered 3D mesoporous silicate with cubic Ia3d

✉ Gamze Gunduz-Meric
gamze.gunduz@bilecik.edu.tr

[1] Chemical Engineering Department, Bilecik Seyh Edebali University, 11230 Bilecik, Turkey

symmetry, tunable pore size, improved wall thickness, and excellent thermal/hydrothermal stability can easily incorporate metals such as W and Zr [28]. The study of porous materials containing Zr as solid acid catalysts has received more attention recently. We were motivated to investigate the direct incorporation of Zr species into the mesoporous KIT-6 framework with n-butanol and a suitable zirconium source, utilizing triblock copolymers as the structure-directing agent. Our investigation was based on these reported studies and their benefits. It was shown that the Zr-KIT-6 materials are extremely stable, selective, and active for alcohol dehydration. A potential advantage is that, in comparison to MCM-41-type materials, Zr-KIT-6 materials with tunable pore sizes could provide better pore accessibility due to their large-pore Ia3d-type structure. In this study, effective, low-cost, eco-friendly KIT-6 silicas were synthesized under mild conditions. KIT-6 has physicochemical properties such as a large surface area, a good ability to disperse active phases on catalysts, and good thermal-mechanical resistance [29]. Mesoporous KIT-6 silicas have a la3d cubic structure with cylindrical pores and large 3-D mesopores with open channels, so they show efficient catalytic capacity.

The synthesis and characterization of Zr-based KIT-6 silicas and their H_2O_2 decomposition capacities were reported. In mild conditions, high H_2O_2 decomposition capacity was observed. It is important to be suitable for all conditions. For the decomposition of H_2O_2, the combination of the high specific surface area and the metal particles in the KIT-6 was very important [30]. The researcher wishes to investigate the incorporation of Zr ions into KIT-6 under the hydrothermal method using triblock copolymer P123 in the n-butanol solvent for the reaction. Zr-containing mesoporous silicas have great consideration in most reactions and processes because of their effective, recyclable, and green material properties [31, 32]. The present work is focused on investigating the activity and selectivity of Zr@KIT-6 materials and on establishing the stability of such materials, employing the catalytic decomposition of hydrogen peroxide as a test reaction. It is obvious that developing such a type of activity is key to their possible application as solid acid catalysts for significantly larger substrates. In the following studies, it is aimed to use the decomposition by-products for fuel-cell systems. The Zr-based KIT-6 silicas were characterized by Transmission electron microscopy (TEM), Scanning electron microscopy (SEM), Fourier transform infrared spectroscopy (FT-IR), Ammonia temperature-programmed desorption (NH_3-TPD), Hydrogen temperature-programmed reduction (H_2-TPR), N_2 adsorption–desorption, X-ray diffraction (XRD) and Inductively coupled plasma-optical emission spectrometry (ICP-OES) analysis.

2 Experimental section

2.1 Synthesis of Zr based KIT-6 silicas

Zr@KIT-6 silicas with different metal contents were prepared by the typical procedure [33]. Zr containing KIT-6 mesoporous la3d structure materials with Si/metal 1.25, 2.5, 5, 10 wt % were synthesized using Pluronic P123 (Carbosynth) tri-block copolymer and n-butanol (Merck). 5.0 g of P123 was dissolved in 161 ml of 0.5 M hydrochloric acid (Merck) at 35 °C. After dissolution was completed, 5.0 g of n-butanol was added and the resulting mixture was stirred for 1 h at 35 °C. Metal source Zr (Sigma-Aldrich) and the required amounts of TEOS (Abcr) were added to the mixture to obtain the desired molar ratio of 1.25, 2.5, 5, and 10 wt % and the mixture was stirred for 24 h. Finally, the reaction mixture was poured into a 250 ml Teflon autoclave for hydrothermal treatment (24 h at 100 °C). The final solid was separated and dried at 100 °C overnight. The directing agent was removed by calcination in dry air at 550 °C for 5 h.

2.2 Characterizations

The surface morphology of Zr-loaded KIT-6 mesoporous silicas was measured by TEM; JEOL 1220 JEM and SEM; Zeiss Supra 40 V device. The textural parameters (specific surface areas, porosities, and pore sizes) were obtained via N_2 adsorption–desorption isotherms using BET and BJH methods (Micromeritics ASAP instrument). Before the measurements samples were outgassed at 250 °C and 100 mmHg, overnight. FT-IR spectra of all the samples were recorded on a Cary 630 Fourier transform infrared spectrometer, equipped with a single reflection diamond attenuated total reflectance (ATR) accessory between 400 and 4000 cm^{-1} employing diluted samples. XRD patterns of the samples were obtained by a Panalytical Empyrean instrument at 200 kV and 50 mA with 2Θ values ranging between 5 and 80° and with a speed of 10 °C/min. Metal loading was determined from ICP-OES analyses; Perkin Elmer Optima 4300DV. To determine the distribution of acid sites of the samples, the temperature-programmed desorption of ammonia (NH_3-TPD) was carried out in Autochem II-2920, Micromeritics. Before NH_3-TPD, 100 mg of samples were heated from room temperature to 250 °C to remove adsorbed water and cooled suddenly to 50 °C in a flow of helium (20 cm^3 min^{-1}). The samples were saturated with a flow of 15 (v/v) % NH^3 in He at 50 °C. Subsequently, NH_3 was desorbed in a He flow of 25 cm^3 min^{-1} up to a temperature of 700 °C with a ramp rate of 10 K min^{-1}, and the desorbed ammonia was recorded.

Temperature-programmed reduction with H_2 (H_2-TPR) of the samples was carried out in a Micromeritics Autochem II-2920. Before H_2-TPR, 100 mg of samples were heated from room temperature to 600 °C with a ramp rate of 10 K min^{-1} in a He flow of 25 cm^3 min^{-1} and cooled suddenly to 50 °C in a flow of helium (20 cm^3 min^{-1}). Typically, TPR experiments were performed with a 5% H_2 in Ar flow (50 cm^3 min^{-1}) heating from 50 to 900 °C at a ramp rate of 10 °C min^{-1}. The H_2 consumption was determined by a TCD detector.

2.3 Decomposition of H_2O_2

The catalytic decomposition of H_2O_2 was performed in a standard volumetric flask including 5.5 g H_2O_2 (30%), 0.25 g material and the temperature is ~ 25 °C with stirring for 2 h. After that, 10 mL of the above solution was withdrawn at different time intervals and then titrated with a standard KMnO4 solution after the addition of 20 ml of 2 M H_2SO_4 and 20 ml of water to determine the concentration of the remaining H_2O_2 [34]. Also, a control test was performed without a catalyst at the same reaction condition. The H_2O_2 decomposition conversion was determined by the following Eq. (1):

$$\%\, H_2O_2 \text{ conversion} = 100 \times \left(a_o - a_t\right)/a_o \quad (1)$$

where a_o is the initial concentration of H_2O_2 and it is the concentration of H_2O_2 at the time (t). The catalytic stability of the KIT-6 silicas was investigated by a recycling test for four simultaneous reactions. After each H_2O_2 decomposition reaction, the catalyst was filtered, washed, dried, and then reused with a fresh H_2O_2 solution.

3 Results and discussion

3.1 Characterization of catalysts

Textural data for materials is illustrated in Table 1. Results indicated higher surface areas for KIT-6 silicas synthesized by this method. The BET-specific surface area decreased as the Zr content increased, going from 780 to 739 m^2/g, respectively. This is explained by the possibility that Zr_2O_5 small clusters, which affect the KIT-6 structure, develop in the mesoporous channels of KIT-6. Pore volumes varied between 0.6 and 1.0 cm^3/g. It is thought that the reason for the change in pore volumes may be the metal distribution near the surface rather than inside the pores. It is also seen that this change may occur due to metal losses in the structure. Pore diameters varied between 4.5 and 5.5 nm. These sizes were in the vicinity of the threshold determining mesoporous structure. ICP-OES results indicated a loss of active Zr metal during synthesis (Table 1). It is thought that the metal percentage might be lost during the synthesis procedure or passed into the washing water during the washing procedure.

The surface morphology of Zr@KIT-6 silicas was investigated by SEM images (Fig. 1). The spongy, porous structure of KIT-6 was shown in the images. Zirconium ions in the network affected the surface smoothness of the materials and agglomerated into small, irregular particles. The morphology of the materials was also determined by TEM analysis (Fig. 2).

It was confirmed by HR-TEM images (Fig. 2) that Zr@KIT-6 silica, such as KIT-6, possesses Ia3d cubic structure and that these channels are well-ordered cubic 3D mesoporous. TEM images confirmed these ordered pore structures consistent with other metal-incorporated KIT-6 materials. The result exhibited the well-ordered arrays of mesoporous channels and well-ordered pore structures of mesopores.

The structural properties of Zr@KIT-6 silicas were measured between 4000−400 cm^{-1} with FT-IR (Fig. 3a). The characteristic peak of the Si-O-Si bond appeared at about 1074 cm^{-1} for all samples due to symmetrical stretching vibrations. The peaks at 455 cm^{-1} and 806 cm^{-1} correspond to the bending of the Si–O bond and the asymmetrical bending of the Si–O–Si bond, respectively. Symmetric stretching of Si–OH was observed around 952 cm^{-1}. Besides the band at about 3392 cm^{-1}, the peaks around 1645–1650 cm^{-1} show –OH stretching vibrations related to adsorbed water molecules that readily allow surface modification [25], [31], [35, 36]. The results were similar to our previous study [10]. The calcined KIT-6's FTIR spectrum showed a broad band at 3467 cm^{-1}, which was caused by defective –OH groups and water's –OH stretching vibration (Fig. 3b). The bending vibration of water occurred at 1642 cm^{-1}. At 1083 cm^{-1},

Table 1 Textural data of Zr@KIT-6 silicas

Catalyst	S_{BET} (m^2/g)	V_{pore} (cm^3/g)	Pore size (nm)	ICP-OES (% loss)
Si/Zr: 10 KIT-6(1)	780.3	0.6	4.5	7.2
Si/Zr: 5 KIT-6(2)	763.7	1.0	4.7	3.8
Si/Zr: 2.5 KIT-6(4)	742.8	0.8	4.9	2.0
Si/Zr: 1.25 KIT-6(8)	738.7	0.7	5.5	1.1

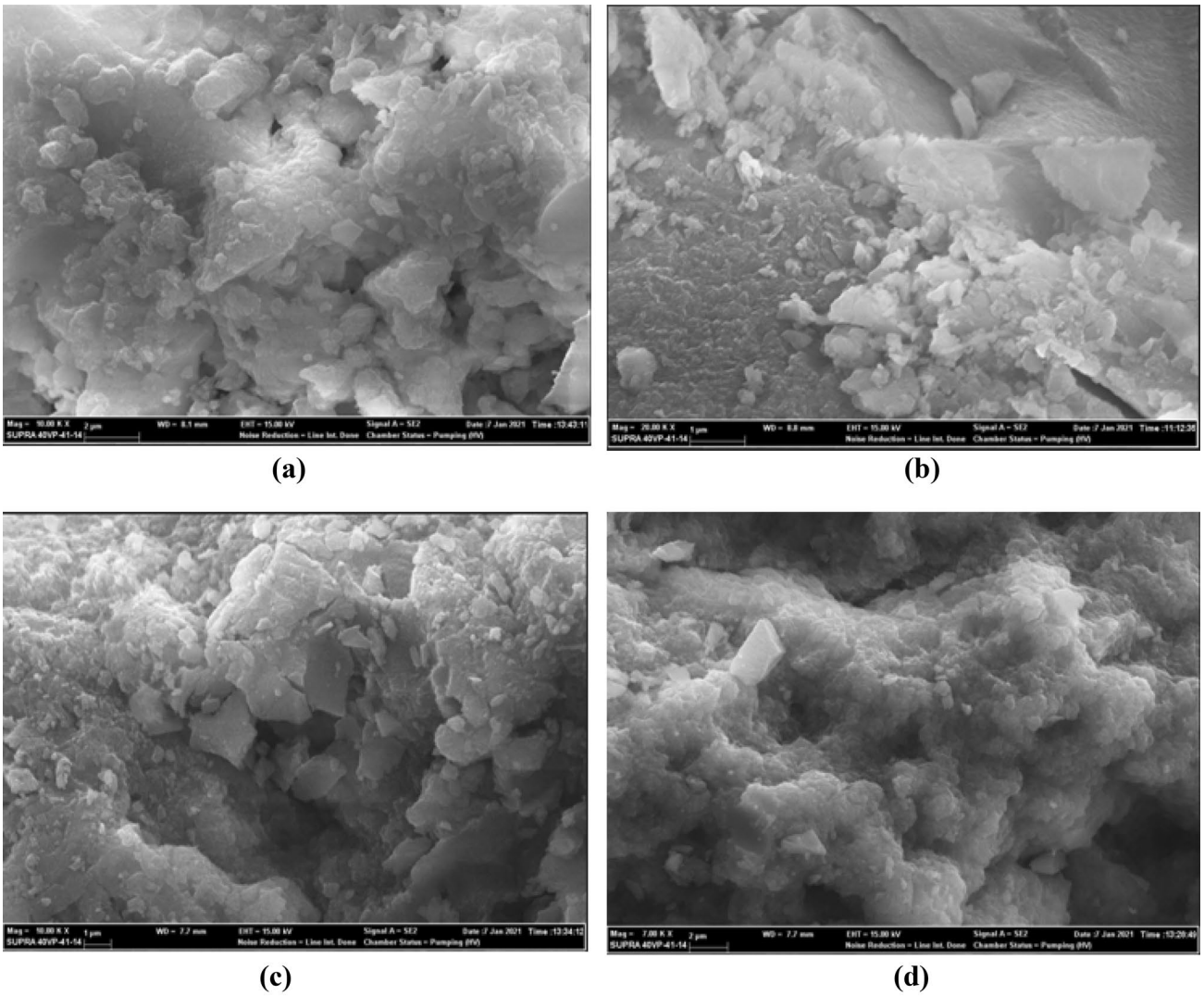

Fig. 1 SEM images of **a** Si/Zr: 10 KIT-6, **b** Si/Zr: 5 KIT-6, **c** Si/Zr: 2.5 KIT-6, **d** Si/Zr: 1.25 KIT-6 (20.00 KX)

the asymmetric Si–O–Si stretching vibration gave an intense broadband. At 956 cm^{-1}, the defective Si–O–H stretching vibration produced a well-defined peak. Si–O–Si groups showed symmetric stretching and bending vibrations at 799 and 463 cm^{-1}, respectively.

The reducibility of the materials was examined by H_2-TPR analysis. Figure 4 presents H_2-TPR profiles of samples, including KIT-6 and Zr@KIT-6. In TPR profiles, reduction peaks of reducible metal oxide structures in materials are shown at different time intervals at increasing temperature due to H_2 consumption. Two distinct H_2 consumption peaks were found around 500 and 600 °C for the Si/Zr:10 KIT-6. This corresponds to the progress of the material in two-stage reduction [37]. The low-temperature H_2 consumption peak is more severe than the high-temperature consumption peak [38]. Looking at the H_2 consumption of the Si/Zr:5 KIT-6, two distinct peaks were observed at approximately 450 and 700 °C. Here, too, there is a two-stage reduction. Multiple reduction peaks indicate that each corresponds to another oxide. The higher the interaction activity with the support material, the more the reduction temperature varies. It appears that KIT-6 does not exhibit a reduction peak, suggesting that Zr_2O_5 reduction was the cause of all H_2 consumption peaks. According to the reduction peak of H_2-TPR profiles of Zr@KIT-6, reducible Zr_2O_5 can be divided into three stages, α-, β-, and γ-stages, corresponding to low-, mid-, and high-temperature peaks. Bulk Zr_2O_5 reduction was attributed to the β-stage at 450–500 °C, which indicates a stronger interaction between Zr species and KIT-6. The presence of Zr silicate and small Zr_2O_5 nanoparticles, which strongly interacted with KIT-6, caused the γ-stage at 600–700 °C. Also, the reducible behavior of the catalyst was remarkably affected by the preparation process at the synthesis stage. Si/Zr:10 KIT-6's high-temperature

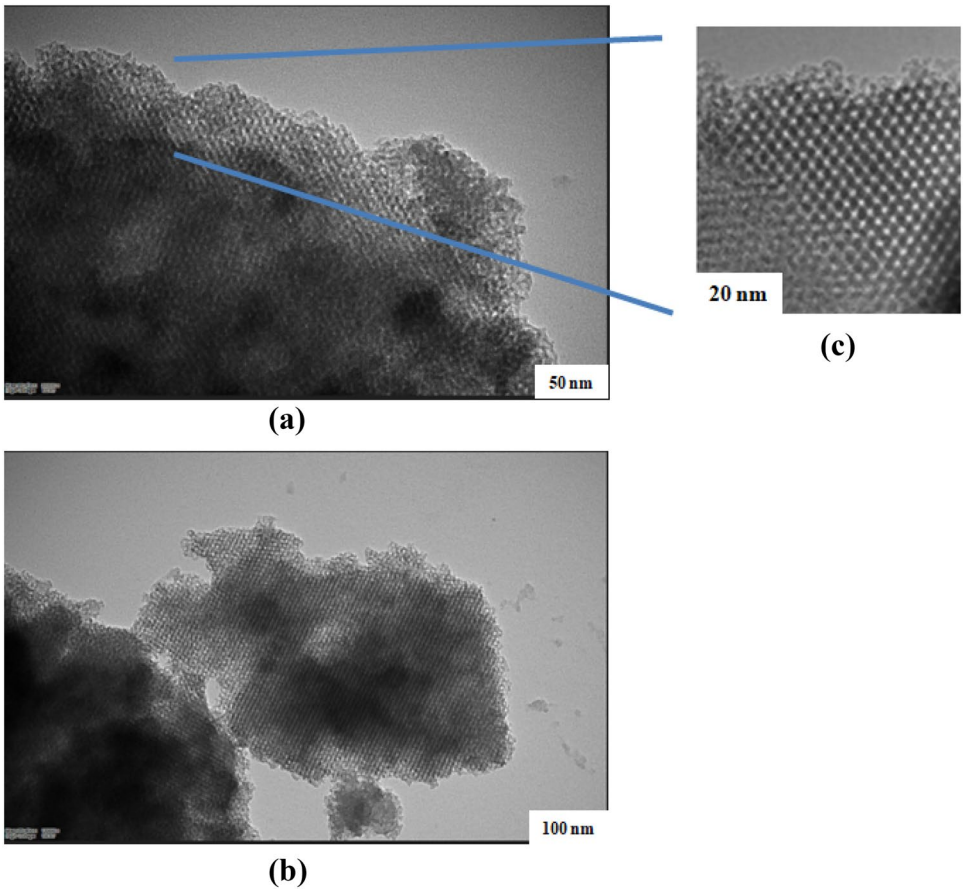

Fig. 2 High-resolution TEM images of **a** (200.00 KX), **b** (120.00 KX), **c** (400.00 KX) Zr@KIT-6 silicas

peak was lower than that of another catalyst, indicating that the Zr species' weakening interaction with KIT-6 facilitated Zr_2O_5's reducibility. The formation of Zr nanoparticles was greatly affected by the confinement effect of 3D-mesopores, which controlled Zr nanoparticles in a defined space and hence limited their size.

Base molecules are adsorbed more strongly in strong centers than in weak centers. Therefore, more energy or higher temperature is required for the desorption of molecules adsorbed in strongly acidic centers. The acid sites in Zr@KIT-6 materials were quantified by NH_3-TPD measurements and the results are shown in Fig. 5. NH_3-TPD analyzes were performed on the silicas that gave the best reaction results. Basically, two peaks are seen in the spectrum obtained in this way. Low temperature peaks for both materials correspond to ammonia desorbed from weak centers. High temperature peaks correspond to strong centers. By analyzing the ammonia desorption curves, the force distributions of the acid centers of the materials were obtained [39]. The NH_3-TPD data for KIT-6 show essentially no features, indicating that the surface acid density of this material was extremely low. While low acidities were measured for Zr@KIT-6 samples, significantly greater acidities were observed in the samples. The measured total acidity increased with Zr content. Lewis acid sites are considered to be responsible for the low-temperature peaks, which are characterized by weak acid sites centered at 50–150 °C. A significant amount of ammonia was desorbed at temperatures above 400 and 500 °C, suggesting that Zr@5 KIT-6 materials also possess strong acid sites that arise from the Brønsted acid sites. Zr@KIT-6 generated NH_3 desorption peaks at 50–150 °C and 400–600 °C, which indicate weak and strong acid sites, respectively.

High angle XRD patterns of Zr@KIT-6 silicas and low angle XRD pattern of the calcined KIT-6 are given in Fig. 6. As seen in Fig. 6a, characteristic peaks of zirconium could not be detected in Zr-containing KIT-6 silicas. The reason for this is thought to be due to the homogeneous distribution of the loaded zirconium in the structure or because it contains zirconium at such a low intensity that it cannot be measured in the analysis. It is known that the peaks seen at 2Θ: 20–30° in all materials originate from the amorphous silica structure. Figure 6b shows the low-angle X-ray diffraction pattern of the calcined KIT-6. The XRD pattern displays a hump for the (220) plane and a sharp, strong peak at $2\theta = 1.06$, it corresponds to the (211) plane. The material's well-ordered mesoporous structure and presence in the bicontinuous cubic space group Ia3d are both made

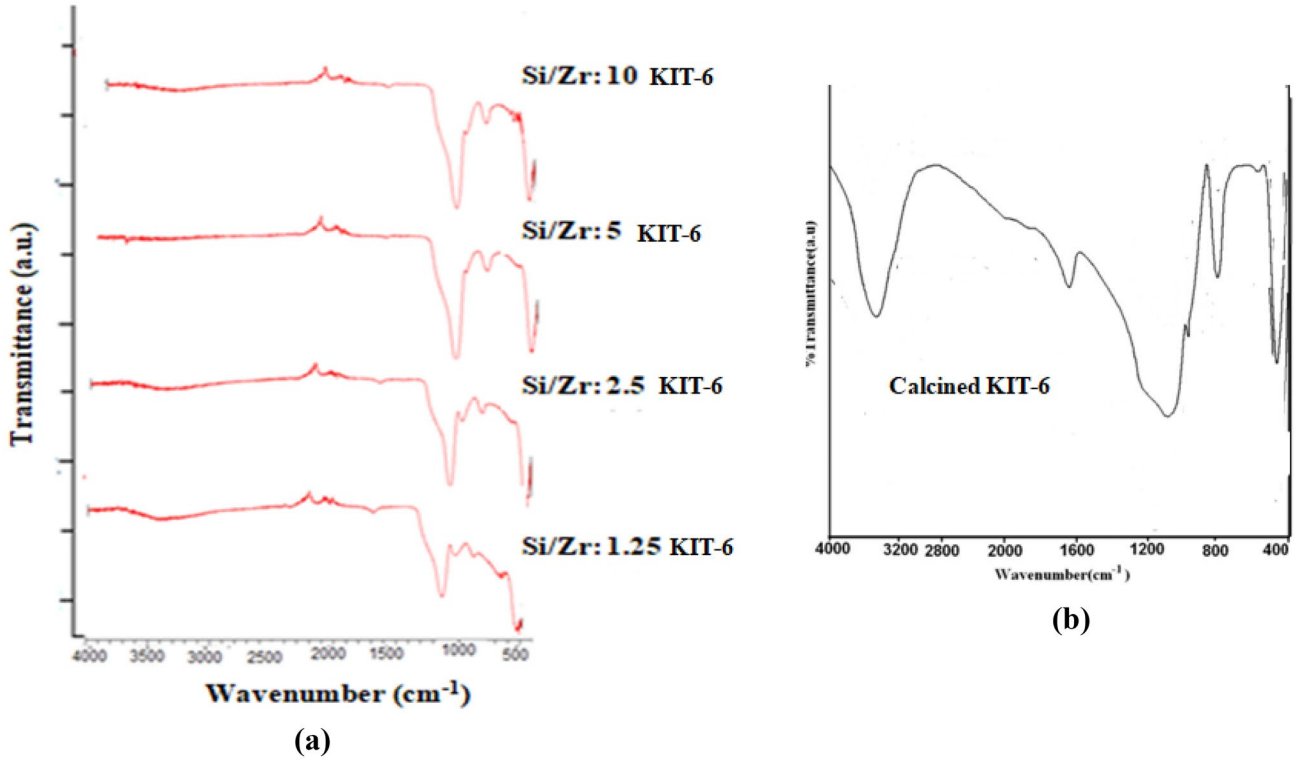

Fig. 3 FT-IR spectra of **a** Zr@KIT-6 silicas, **b** calcined KIT-6

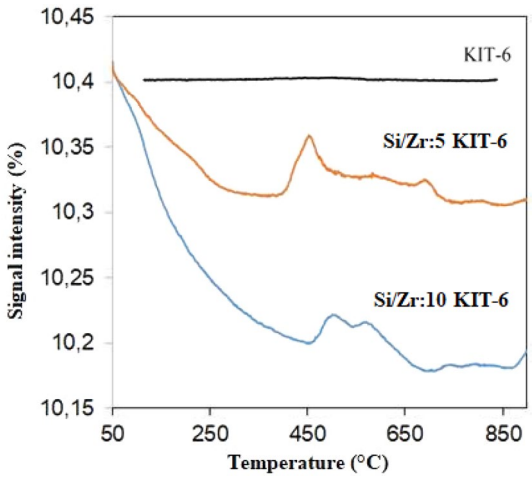

Fig. 4 H_2-TPR profiles of KIT-6 silicas

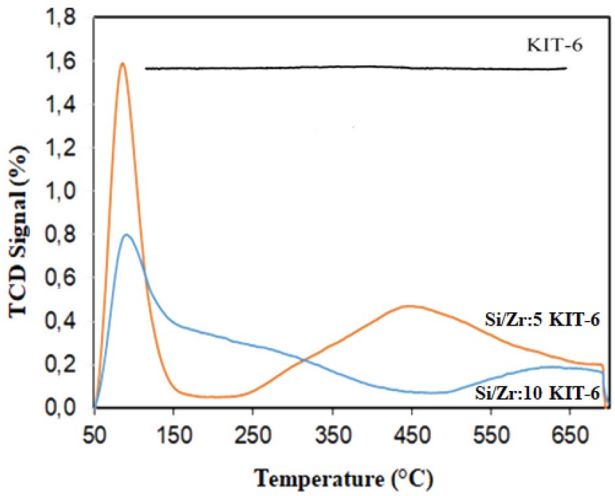

Fig. 5 NH_3-TPD profiles of Si/Zr: 5, Si/Zr:10 KIT-6 silicas

clear by the XRD pattern. The results of the calculation of the calcined silica show that it is KIT-6 with body-centered cubic symmetry, with dimensions of 203.9 Å (211) and 177 Å (220), which are in good accord with previous results reported in the literature [25].

The mesoporous structure of KIT-6 supported materials was investigated using N_2 adsorption desorption analysis. The nitrogen capillary condensation plays a role in the Type IV behavior shown in the N_2 adsorption–desorption isotherms of the Zr@KIT-6 samples (Fig. 7), which show a sharp inflection at a relatively high partial pressure of 0.6–0.8. According to the IUPAC classification of the materials, it has been shown that they comply with the type IV isotherm, which shows the adsorption/desorption isotherm behavior of microporous solids containing mesopores [40].

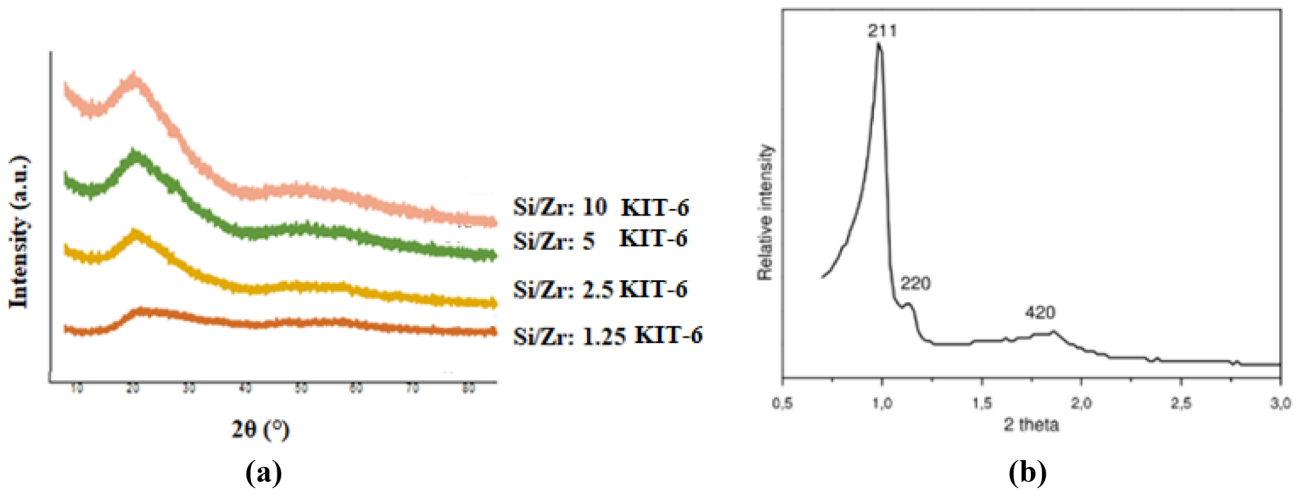

Fig. 6 **a** High angle XRD diffraction patterns of Zr@KIT-6 silicas, **b** Low angle XRD diffraction pattern of the calcined KIT-6

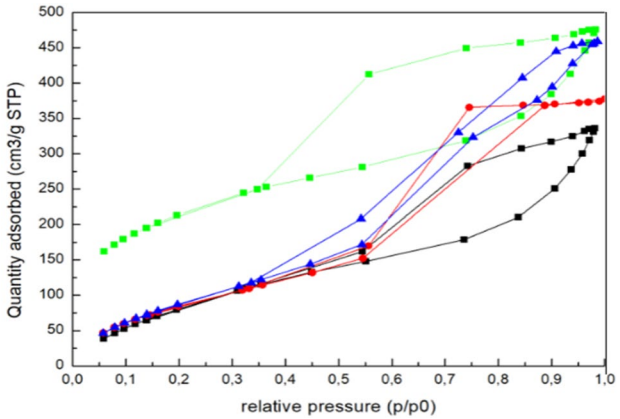

Fig. 7 N_2 adsorption–desorption isotherms for Zr@KIT-6 silicas (blue: Si/Zr:1.25 KIT-6, red: Si/Zr:2.5 KIT-6, green: Si/Zr:5 KIT-6, black: Si/Zr:10 KIT-6)

The uniformity of pores is indicated by the H1-type hysteresis loop that is observed in all Zr@KIT-6 samples.

3.2 Catalytic performance of the catalysts and reusability test

Decomposition of H_2O_2 reactions were conducted in the presence of Zr based KIT-6 silicas at mild conditions. H_2O_2 was introduced to a standard volumetric flask containing 0.25 g catalyst. Results were illustrated in terms of H_2O_2 conversion (Fig. 8). H_2O_2 conversions at the end of 2 h were determined as 63%, 70%, 82% and 91% for 1.25, 2.5, 5 and 10 Si/Zr KIT-6 silicas. The synthesized silicas in this study have shown good catalytic activity for H_2O_2 decomposition reaction. It is obvious from reaction experiments that 5 and 10 Si/Zr KIT-6 silicas had the highest activity

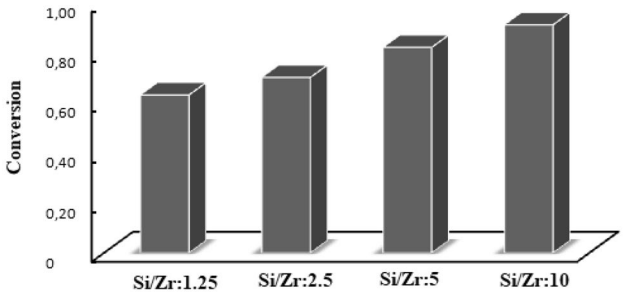

Fig. 8 The decomposition of H_2O_2 at 25 °C using Zr@KIT-6 silicas

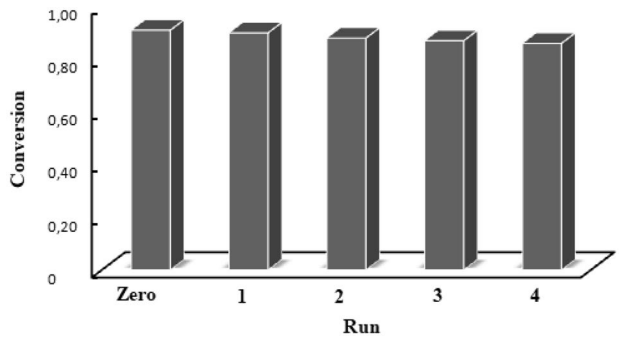

Fig. 9 The reusability performance of Si/Zr:10 KIT-6 silica towards decomposition of H_2O_2

among those synthesized by varying Zr amounts. For industrial applications the reusability and stability of the catalyst are very important. The highest active 10% Si/Zr catalyst was selected to reusability performance for 4 times at same conditions (Fig. 9). This catalyst was seperated from reaction mixture by centrifugation. The catalyst could have been

used without any significant loss. The catalytic activity was slightly reduced from 91 to 86% after 4 times usage. It was observed that the Zr@KIT-6 silicas exhibited higher stability in H_2O_2 decomposition. There is no significant decrease in catalytic efficiency after 4 consecutive runs. The catalysts synthesized in this study have shown good catalytic activity for decomposition of H_2O_2 reaction. Reaction studies were conducted in the presence of a variety of catalysts with varying experimental conditions and selected studies were summarized in Table 2. It was clearly seen from the table that synthesized catalyst had been among the ones with highest activity and efficiency.

3.3 Kinetic study

The kinetics of the decomposition of H_2O_2 at room temperature over Zr@KIT-6 silicas were studied. The pseudo first order kinetics for H_2O_2 decomposition reaction was confirmed by the literature [44, 45]. The plotting of −ln(1-X) as a function of time (t) (Fig. 10) (2)

$$-\ln(1-X) = kt. \quad (2)$$

The graph showed linear nature with correlation coefficient (R^2) value higher than 0.99. This excellent linearity emphasizes the pseudo first-order kinetics for H_2O_2 decomposition reaction. The pseudo first order rate constant from the graph was found to be 0.066 min^{-1} at 25 °C.

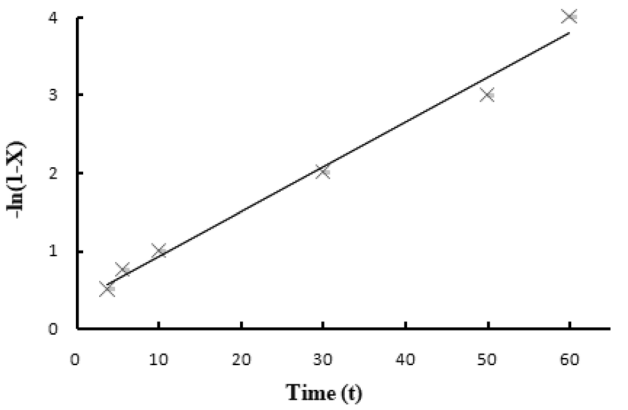

Fig. 10 First-order plot of H_2O_2 decomposition on Si/Zr:10 KIT-6 silica at 25 °C

4 Conclusions

Direct hydrothermal synthesis using pluronic P123 and n-butanol as the structure-directing agent was successful in generating cubic three-dimensional Zr@KIT-6 materials with Ia3d symmetry and different Si/Zr atomic ratios. The results of high-resolution TEM and N_2 sorption clearly showed the presence of a highly ordered cubic structure. The Zr@KIT-6 samples have mostly weak and strong acid sites, which vary almost linearly with Zr content, according to NH_3-TPD measurements. The total acidity of Zr@KIT-6 materials increased with zirconium content. For the decomposition of hydrogen peroxide, high activity (91%) and stability were displayed in the mild conditions. Based the reusability performance, it is concluded that Si/Zr:10 KIT-6 silica is stable. The catalytic activity was slightly reduced from 91 to 86% after four run. The results presented here demonstrate that Zr-KIT-6 materials are efficient acidic catalysts with high activity and durability that could be potentially exploited in the decomposition of various substrates. The availability of such catalysts for environmental applications could be especially advantageous to the developing renewable chemicals industry.

Table 2 Literature comparison of the synthesized catalyst in similar conditions

Researcher	Catalyst	Reaction conditions	Conversion
Mahmoud et al. (2019) [41]	MnSnO	20 °C, 1 h, 0.1 g catalyst	84.4%
Mahmoud et al. (2022) [42]	M/BS@Ag core-shell nanoparticles	20 °C, 1 h, 0.1 g catalyst	95%
Maurya et al. (2002) [34]	[Fe(salpn)]-Y	25 °C, 2 h, 0.025 g catalyst	45.69%
Kwon et al. (2018) [43]	MnO_2/GAC	25 °C, 1 h, 5 g catalyst	85%
This work	Si/Zr@KIT-6	25 °C, 2 h, 0.25 g catalyst	91%

Acknowledgements Bilecik Seyh Edebali University, Yıldız Technical University Central Research Laboratories and Sivas Cumhuriyet University Chemical Engineering Department Laboratuary are gratefully acknowledged for characterization studies. Part of the study was supported by the BAP 2019-02.BŞEU.03-04 project.

Author contributions The author investigated the study, wrote original draft, contributed the study conception and design, commented the characterization studies.

Funding Not applicable.

Declarations

Conflict of interest The author declares that they have no known competing financial interests or personal relationships that could have appeared to influence the work reported in this paper.

Consent to participate Not applicable.

Consent to publish Not applicable.

Ethical approval Not applicable.

References

1. C.W. Jones, J.H. Clark, Introduction to the preparation and properties of hydrogen peroxide. Appl. Hydrog. Peroxide Deriv. (1999). https://doi.org/10.1039/9781847550132-00001
2. D.J. Weber et al., Effectiveness of ultraviolet devices and hydrogen peroxide systems for terminal room decontamination: focus on clinical trials. Am. J. Infect. Control. **44**(5), e77–e84 (2016)
3. Y. Zhang et al., Activation of persulfate by core–shell structured Fe_3O_4@ C/CDs-Ag nanocomposite for the efficient degradation of penicillin. Sep. Purif. Technol. **254**, 117617 (2021). https://doi.org/10.1016/j.seppur.2020.117617
4. C. Vivek, B. Balraj, S. Thangavel, Structural, optical and electrical behavior of ZnO@ Ag core–shell nanocomposite synthesized via novel plasmon-green mediated approach. J. Mater. Sci. **30**(12), 11220–11230 (2019). https://doi.org/10.1007/s10854-019-01467-x
5. E.A. Bakr et al., Facile synthesis of superparamagnetic Fe_3O_4@ noble metal core–shell nanoparticles by thermal decomposition and hydrothermal methods: comparative study and catalytic applications. RSC Advances **11**(2), 781–797 (2021). https://doi.org/10.1039/d0ra08230a
6. J. Scarıa, A. Gopınath, P.V. Nıdheesh, A versatile strategy to eliminate emerging contaminants from the aqueous environment: Heterogeneous Fenton process. J. Clean. Prod. **278**, 124014 (2021). https://doi.org/10.1016/j.jclepro.2020.124014
7. R. Turco et al., Sintered metal fibers coated with transition metal oxides as structured catalysts for hydrogen peroxide decomposition. Chem. Eng. Process. **73**, 16–22 (2013). https://doi.org/10.1016/j.cep.2013.08.004
8. C.Ã.M. Lousada et al., Catalytic decomposition of hydrogen peroxide on transition metal and lanthanide oxides. J. Mol. Catal. A **379**, 178–184 (2013). https://doi.org/10.1016/j.molcata.2013.08.017
9. G.M. Gamze, Fe/KIT-6 Katalizörlerinin Sentezi, Karakterizasyonu ve H_2O_2 Bozunma Reaksiyonunda Aktivitelerinin İncelenmesi. Afyon Kocatepe Üniversitesi Fen Ve Mühendislik Bilimleri Dergisi **21**(2), 442–448 (2021). https://doi.org/10.35414/akufemubid.865113
10. G.M. Gamze, Catalytic decomposition of H_2O_2 over Nb/KIT-6 catalyst for environmental applications. React. Kinet. Mech. Catal. **135**(4), 2059–2071 (2022). https://doi.org/10.1007/s11144-022-02235-5
11. D. Gudarzı et al., Factors affecting catalytic destruction of H_2O_2 by hydrogenation and decomposition over pd catalysts supported on activated carbon cloth (ACC). Catal. Today. **248**, 69–79 (2015). https://doi.org/10.1016/j.cattod.2013.12.050
12. S. Amırfakhrı, Javad et al., Investigation of hydrogen peroxide reduction reaction on graphene and nitrogen doped graphene nanoflakes in Neutral solution. J. Power Sources. **257**, 356–363 (2014). https://doi.org/10.1016/j.jpowsour.2014.01.114
13. J. LI et al., Theoretical study of the decomposition and hydrogenation of H_2O_2 on pd and Au@ pd surfaces: understanding toward high selectivity of H_2O_2 synthesis. J. Phys. Chem. C **115**(15), 7392–7398 (2011). https://doi.org/10.1021/jp1070456
14. J.M. Campos-Martın, G. Blanco-Brıeva, L.G. Fıerro, Jose, Hydrogen peroxide synthesis: an outlook beyond the anthraquinone process. Angew. Chem. Int. Ed. **45**(42), 6962–6984 (2006). https://doi.org/10.1002/anie.200503779
15. Y. Voloshın, J. Manganaro, A. Lawal, Kinetics and mechanism of decomposition of hydrogen peroxide over Pd/SiO_2 catalyst. Ind. Eng. Chem. Res. **47**(21), 8119–8125 (2008). https://doi.org/10.1021/ie8000452
16. K.M. Marr et al., High aspect ratio carbon nanotube membranes decorated with pt nanoparticle urchins for micro underwater vehicle propulsion via H_2O_2 decomposition. ACS nano. **9**(8), 7791–7803 (2015). https://doi.org/10.1021/acsnano.5b02124
17. B. Chen et al., Platinum nanoparticle decorated SiO_2 microfibers as catalysts for micro unmanned underwater vehicle propulsion. ACS Appl. Mater. Interfaces. **845**, 30941–30947 (2016). https://doi.org/10.1021/acsami.6b10047
18. D. Krejcı et al., Structural impact of honeycomb catalysts on hydrogen peroxide decomposition for micro propulsion. Chem. Eng. Res. Des. **90**(12), 2302–2315 (2012). https://doi.org/10.1016/j.cherd.2012.05.015
19. A. Unnarkat, A. Namdeo, R. Bhoi, Bimetallic catalyzed decomposition of hydrogen peroxide–Kinetics, effect of support and reaction medium. Mater. Today **45**, 5183–5189 (2021)
20. V. Parvulescu, B.L. Su, Iron, cobalt or nickel substituted MCM-41 molecular sieves for oxidation of hydrocarbons. Catal. Today. **69**(1–4), 315–322 (2001)
21. A. Namdeo, S.M. Mahajani, A.K. Suresh, Palladium catalysed oxidation of glycerol—effect of catalyst support. J. Mol. Catal. A. **421**, 45–56 (2016)
22. A.K. Suresh, T. Sridhar, O.E. Potter, Catalyzed oxidation of cyclohexane in the liquid phase. AIChE J. **36**(1), 137–140 (1990)
23. V.R. Choudhary, C. Samanta, P. Jana, Decomposition and/or hydrogenation of hydrogen peroxide over Pd/Al_2O_3 catalyst in aqueous medium: factors affecting the rate of H_2O_2 destruction in presence of hydrogen. Appl. Catal. A **332**(1), 70–78 (2007). https://doi.org/10.1016/j.apcata.2006.10.022
24. Y. Lee, Ng et al., Hydrogen peroxide decomposition over Ln1 – xA_xMnO_3 (ln = La or Nd and A = K or Sr) perovskites. Appl. Catal. A **215**(1–2), 245–256 (2001). https://doi.org/10.1016/S0926-860X(01)00536-1
25. A. Ramanathan et al., Niobium incorporated mesoporous silicate, Nb-KIT-6: synthesis and characterization. Microporous Mesoporous Mater. **190**, 240–247 (2014). https://doi.org/10.1016/j.micromeso.2014.02.019
26. A. Ramanathan et al., Synthesis and characterization of Zirconium incorporated Ultra large pore mesoporous silicate, Zr–KIT-6. Microporous Mesoporous Mater. **167**, 207–212 (2013). https://doi.org/10.1016/j.micromeso.2012.09.008

27. D.-. Hua et al., Synthesis of mesoporous MCM-48 molecular sieves of high quality in a fluorine-containing system. J. fuel Chem. Technol. **40**(5), 564–568 (2012). https://doi.org/10.1016/S1872-5813(12)60023-1
28. Q. Pan, A. Ramanathan, W.K. Snavely, R.V. Chaudhari, B. Subramaniam, Synthesis and dehydration activity of novel Lewis acidic ordered mesoporous silicate: Zr-KIT-6. Ind. Eng. Chem. Res. **52**(44), 15481–15487 (2013)
29. R. Kıshor, A. Ghoshal, Kumar, Understanding the hydrothermal, thermal, mechanical and hydrolytic stability of mesoporous KIT-6: a comprehensive study. Microporous Mesoporous Mater. **242**, 127–135 (2017). https://doi.org/10.1016/j.micromeso.2017.01.020
30. W. Wang et al., Synthesis of KIT-6 type mesoporous silicas with tunable pore sizes, wall thickness and particle sizes via the partitioned cooperative self-assembly process. Microporous Mesoporous Mater. **194**, 167–173 (2014). https://doi.org/10.1016/j.micromeso.2013.10.028
31. H. Lıu et al., Enhanced catalytic performance for metathesis reactions over ordered tungsten and aluminum co-doped mesoporous KIT-6 catalysts. New J. Chem. **39**(10), 7971–7978 (2015). https://doi.org/10.1039/C5NJ01415H
32. C. Jo, K. Kım, R. Ryoo, Syntheses of high quality KIT-6 and SBA-15 mesoporous silicas using low-cost water glass, through rapid quenching of silicate structure in acidic solution. Microporous Mesoporous Mater. **124**(1–3), 45–51 (2009). https://doi.org/10.1016/j.micromeso.2009.04.037
33. N.M. Ghohe, R. Tayebee, M.M. Amını, Synthesis and characterization of mesoporous NbZr/KIT-6 as a productive catalyst for the synthesis of benzylpyrazolyl coumarins. Mater. Chem. Phys. **223**, 268–276 (2019). https://doi.org/10.1016/j.matchemphys.2018.10.067
34. M.R. Maurya et al., Zeolite-encapsulated cr (III), Fe (III), ni (II), zn (II) and Bi (III) salpn complexes as catalysts for the decomposition of H_2O_2 and oxidation of phenol. J. Mol. Catal. A **180**(1–2), 201–209 (2002). https://doi.org/10.1016/S1381-1169(01)00435-6
35. M. Anılkumar, W.F. Hoelderıch, Gas phase Beckmann rearrangement of cyclohexanone oxime to ε-caprolactam over mesoporous, microporous and amorphous Nb_2O_5/silica catalysts: a comparative study. Catal. Today. **198**(1), 289–299 (2012). https://doi.org/10.1016/j.cattod.2012.01.043
36. L. Xu, C. Wang, J. Guan, Preparation of acid-base bifunctional mesoporous KIT-6 (KIT: Korea Advanced Institute of Science and Technology) and its catalytic performance in Knoevenagel reaction. J. Solid State Chem. **213**, 250–255 (2014). https://doi.org/10.1016/j.jssc.2014.03.010
37. W.-W. Lıu et al., Study on the effect of metal types in (Me)-Al-MCM-41 on the mesoporous structure and catalytic behavior during the vapor-catalyzed co-pyrolysis of pubescens and LDPE. Appl. Catal. B **129**, 202–213 (2013). https://doi.org/10.1016/j.apcatb.2012.09.002
38. R. Wojcıeszak et al., Nickel containing MCM-41 and AlMCM-41 mesoporous molecular sieves: characteristics and activity in the hydrogenation of benzene. Appl. Catal. A **268**(1–2), 241–253 (2004). https://doi.org/10.1016/j.apcata.2004.03.047
39. M.S. Salam, Abdel et al., Synthesis and characterization of MCM-41-supported nano zirconia catalysts. Egypt. J. Pet. **24**(1), 49–57 (2015). https://doi.org/10.1016/j.ejpe.2015.02.005
40. J. Haber, J.H. Block, B. Delmon, Manual of methods and procedures for catalyst characterization (technical report). Pure Appl. Chem. **67**(8–9), 1257–1306 (1995). https://doi.org/10.1351/pac199567081257
41. H.R. Mahmoud, S.A. El-Molla, M.A. Naghmash, Novel mesoporous MnO_2/SnO_2 nanomaterials synthesized by ultrasonic-assisted co-precipitation method and their application in the catalytic decomposition of hydrogen peroxide. Ultrasonics. **95**, 95–103 (2019)
42. H.R. Mahmoud, M. Saif, M.A. Naghmash, Synthesis of M/BS@Ag core-shell nanoparticles (M: Cu, Ni, Co, Fe or Mn ions and BS: $Bi_{12}SiO_{20}$) as novel catalysts for the catalytic decomposition of hydrogen peroxide. J. Phys. Chem. Solids. **161**, 110389 (2022)
43. K.M. Kwon, I.G. Kim, Y.S. Nam, J. Choi, W.I. Cho, I.H. Oh, I.W. Nah et al., Catalytic decomposition of hydrogen peroxide aerosols using granular activated carbon coated with manganese oxides. J. Ind. Eng. Chem. **62**, 225–230 (2018)
44. O. Zeıneb et al., Kinetic study of the catalytic decomposition of H_2O_2 in phosphoric acid medium. Int. J. Hydrog. Energy. **40**(2), 1278–1282 (2015). https://doi.org/10.1016/j.ijhydene.2014.09.144
45. A. Aguınaco et al., Decomposition of hydrogen peroxide in the presence of activated carbons with different characteristics. J. Chem. Technol. Biotechnol. **86**(4), 595–600 (2011). https://doi.org/10.1002/jctb.2560